



arXiv:2505.08843v1 [eess.IV] 13 May 2025

Total Variation-Based Image Decomposition and Denoising for Microscopy Images

Marco Corrias,^{1,2,*} Giada Franceschi,³ Michele Riva,³ Alberto Tampieri,⁴
Karin Föttinger,⁴ Ulrike Diebold,³ Thomas Pock⁵ and Cesare Franchini^{1,6,**}

¹Faculty of Physics and Center for Computational Materials Science, University of Vienna, ²Vienna Doctoral School in Physics, University of Vienna, ³Institute of Applied Physics, TU Wien, ⁴Institute of Materials Chemistry, TU Wien, ⁵Institute of Computer Graphics and Vision, TU Graz and ⁶Department of Physics and Astronomy, University of Bologna

*Marco Corrias, marco.corrias@univie.ac.at **Cesare Franchini, cesare.franchini@univie.ac.at

Abstract

Experimentally acquired microscopy images are unavoidably affected by the presence of noise and other unwanted signals, which degrade their quality and might hide relevant features. With the recent increase in image acquisition rate, modern denoising and restoration solutions become necessary. This study focuses on image decomposition and denoising of microscopy images through a workflow based on total variation (TV), addressing images obtained from various microscopy techniques, including atomic force microscopy (AFM), scanning tunneling microscopy (STM), and scanning electron microscopy (SEM). Our approach consists in restoring an image by extracting its unwanted signal components and subtracting them from the raw one, or by denoising it. We evaluate the performance of TV- L^1 , Huber-ROF, and TGV- L^1 in achieving this goal in distinct study cases. Huber-ROF proved to be the most flexible one, while TGV- L^1 is the most suitable for denoising. Our results suggest a wider applicability of this method in microscopy, restricted not only to STM, AFM, and SEM images. The Python code used for this study is publicly available as part of AiSurf. It is designed to be integrated into experimental workflows for image acquisition or can be used to denoise previously acquired images.

Key words: total variation, image decomposition, denoising, microscopy, AFM, STM, SEM, STEM

Introduction

In recent decades, microscopy has experienced significant advancements, particularly with the advent of scanning probe techniques like scanning tunneling microscopy (STM) (Binnig et al., 1982; Tersoff and Hamann, 1985) and atomic force microscopy (AFM) (Giessibl, 2003; Morita et al., 2015; Pavliček and Gross, 2017). This innovation has revolutionized our ability to explore surface mechanisms at the atomic scale, marking a pivotal breakthrough in the field. Notably, the simultaneous performance of STM and AFM has opened new avenues, allowing for a synergistic exploration of both techniques and enhancing the capabilities for comprehensive surface analysis (Hapala et al., 2015; Dürig et al., 1986; Majzik et al., 2013; Reticioli et al., 2019). Electron microscopy (Inkson, 2016) is a long-established, versatile technique for small-scale investigations, from micro- to nanoscale. Techniques like scanning electron microscopy (SEM), transmission electron microscopy (TEM), and scanning transmission electron microscopy (STEM) allow to investigate the topography and chemical composition of materials by analyzing images generated

from signals due to electron-sample interactions.

Atomically resolved images have the capability to reveal a number of mechanisms and features, encompassing atomic arrangements, molecular adsorption, distribution of defects, and localized charge states such as polarons (Reticioli et al., 2019; Franchini et al., 2021). Experimental investigations at the atomic scale can be further complemented by first-principles calculations, as evidenced by various examples in the literature (Majzik et al., 2013; Spadafora et al., 2014; Stetsovykh et al., 2015; Kraushofer et al., 2021; Meier et al., 2022; Sokolović et al., 2020). This integrated approach not only enhances our understanding of intricate phenomena but also showcases the synergistic interplay between experimental observations and theoretical predictions. It is widely acknowledged that, particularly in small-scale investigations, a significant portion of acquired images exhibits undesirable artifacts and noise, necessitating either their discard or the application of a denoising process (Fan et al., 2019; Elad et al., 2023). The nature of noise varies based on the experimental technique and may encompass Poisson, Gaussian, salt&pepper, or mixed forms.

Consequently, integrating a denoising step into the experimental workflow becomes a standard practice to enhance the quality and reliability of the acquired data. Other than noise, images can display undesirable artifacts due to, for example, tip changes in the case of AFM and electric charge build-up in the case of SEM. These typically low-frequency components also need to be filtered in order to obtain an artifacts- and noise-free image.

For these reasons, a plethora of denoising methods have been developed by the scientific community, which include filters (both in spatial and transform domain), statistical methods and machine learning (Thakur et al., 2021; Goyal et al., 2020). Some of these methods can be partially or fully automated, but occasionally manual filtering might be a more adequate choice. On this regard, popular choices are WSXM (Horcas et al., 2007) or ImageJ (Abràmoff et al., 2004; Collins, 2007) plugins; manual filtering allows for fully controlled denoising and processing but also requires experienced users to perform it. On the other hand, automated signal denoising and processing might require limited knowledge on the topic but also gives less control over the outcome. In conjunction with advancements in microscopy, there has been a simultaneous increase in the volume of data generated during experiments. The manual processes of image selection, denoising, and information extraction are progressively becoming more time-consuming, thereby creating bottlenecks not only for surface science but also for diverse fields such as biology, medicine, and surveillance. Addressing this challenge is crucial to streamline workflows, enhance efficiency, and fully leverage the wealth of information embedded in the expanding datasets. To tackle these challenges, contemporary solutions are imperative, and innovative automated techniques are currently being introduced (Kalinin et al., 2021, 2022; Madsen et al., 2018; Kalinin et al., 2023; Pregowska et al., 2024). Popular choices involve the use of machine learning like convolutional neural networks (Ziletti et al., 2018; Leitherer et al., 2023; Lin et al., 2021), autoencoders (Kingma and Welling, 2019; Chen et al., 2024; Biswas et al., 2023; Alvarado et al., 2023), and other algorithmic strategies (Corrias et al., 2023; Nord et al., 2017; Belianinov et al., 2015; Zhang et al., 2020).

Among many possible denoising methods (Wang et al., 2020; Potapov and Lubk, 2019; Kaur et al., 2018), a popular choice is the total variation (TV) minimization (Chambolle et al., 2010; Chambolle and Pock, 2011) due to its ability to preserve fine details and edges while robustly removing different types of noise, as it allows solutions with discontinuities in the functional space, usually associated with object boundaries. Many applications of TV were discovered during the last decades, such as motion estimation (Werlberger et al., 2010), segmentation (Cai et al., 2019), denoising and deblurring (Liu et al., 2019; Taherkhani et al., 2016). TV denoising itself has been applied to different fields, from hyperspectral imaging for environmental monitoring, agriculture, urban planning (Wang et al., 2021), to spectroscopic (Liao et al., 2015), biological (Chang and Mycek, 2012) and medical (Knoll et al., 2011; Wang et al., 2006) imaging. TV denoising was also applied in the field of microscopy (Kawahara et al., 2022; Meiniel et al., 2018; Chang and Mycek, 2012). Another well-studied application of TV is image decomposition. Image decomposition aims to split an image into its components encoding different types of informations, like structural and textural components (Aujol et al., 2006), oscillatory, harmonic and structural components (Huska et al., 2021), or in general a sum of its constituent ones (Fu et al., 2023). In microscopy imaging, this method can be applied for image restoration, assuming that

images are corrupted by noise and other unwanted signal parts. Moreover, total variation minimization is not affected by image boundary effects caused by popular filtering schemes.

In this work we show how TV denoising and image decomposition can be successfully applied to study cases involving different types of noise and topography, with images obtained from STM, AFM, and SEM experiments. Our study gives practical insights into this methodology and shows its wide degree of applicability on microscopy images, demonstrating it is a valid and non-data-hungry alternative to other modern methodologies. Our results suggest a wider applicability of this method in microscopy, restricted not only to STM, AFM, and SEM images. The Python code used for this study is publicly available on GitHub and is part of the AiSurf (Corrias et al., 2023) package. This code is designed for single- and multiple-image denoising. Importantly, this methodology holds the potential for seamless integration into automated experimental workflows for image acquisition.

Materials and methods

Experimental images

In this study, four different images will be discussed corresponding to four different study cases, which are collected in Fig. 1. Fig. 1a shows a $27 \times 27 \text{ nm}^2$ non-contact AFM image of the UHV-cleaved surface of muscovite mica, exposing undercoordinated K ions (imaged as dark dots) (Franceschi et al., 2023). Image acquired in constant height from top to bottom with a qPlus sensor (Giessibl, 2019) at 4.7 K with a Cu-terminated tip. The lower part of the image appears darker (stronger attractive interaction) than the upper one. This is due to thermal drift: while the acquisition was nominally in the constant-height mode, the tip progressively moved closer to the sample surface while scanning from top to bottom. Both the atomic features and the background are affected. Sporadic low-frequency background changes from one scan line to the next are probably due to electrons (charges) jumping between different sites.

Fig. 1b, shows a $15 \times 15 \text{ nm}^2$ STM image of an A-site rich surface of a (110)-oriented lanthanum-strontium manganite (LSMO) film obtained by annealing at $700 \text{ }^\circ\text{C}$ in UHV for 45 minutes (Franceschi et al., 2021). $V_t = 2.3 \text{ V}$, $I_t = 0.05 \text{ nA}$. The surface features are arranged in zig-zagging rows with a (1×1) periodicity. Sparse, brighter features are assigned to unidentified adsorbates. The sudden, vertical contrast variations (here referred to as 'scratches') are caused by tip changes, likely due to adsorbates attaching and detaching from the tip apex.

Fig. 1c shows a $47 \times 42 \text{ nm}^2$ STM image of a (2×5) -reconstructed $\text{SrTiO}_3(110)$ surface (Riva et al., 2019). $V_t = 1.9 \text{ V}$, $I_t = 0.06 \text{ nA}$. The bright dots aligned along the $[001]$ direction are assigned to Sr atoms, the brighter features appearing in the whole image are unidentified adsorbates. The observed scratches are due to the interaction of the tip with the surface Sr atoms. Horizontal scratches are present due to tip changes. They might originate from an adsorbate picked up from the surface, or other phenomena.

Fig. 1d shows a $8.2 \times 5.5 \text{ } \mu\text{m}^2$ SEM image of a MgAl_2O_4 (spinel) particle. The spinel was synthesized through the combustion method using glycine as a fuel and starting from the corresponding metal nitrates. The obtained solid was ground into powder. The image shows the cleavage surface of the particle, which exposes the material's inner porosity- a common morphology of solids produced through combustion. The image was taken in high

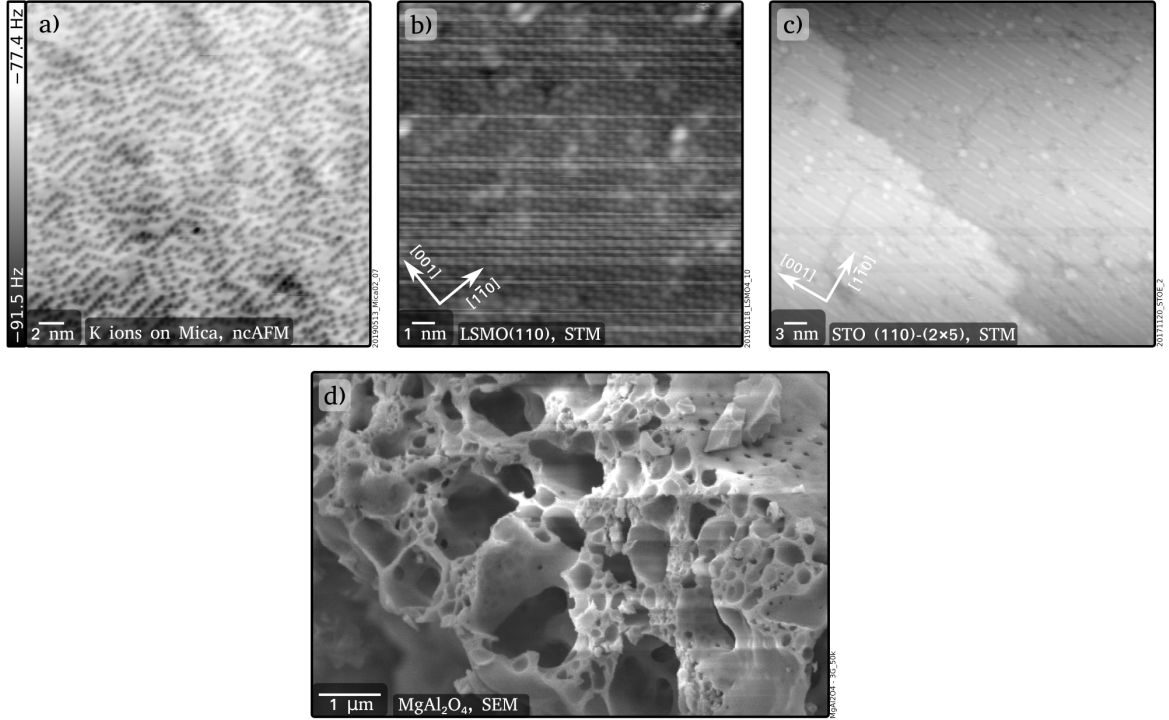


Fig. 1: Experimental images discussed in this study. (a) non-contact AFM image of K ions (imaged as dark dots) on muscovite mica. Adapted with permission (Franceschi et al., 2023). CC BY 4.0, Nature; (b) STM image of an A-site rich surface of a (110)-oriented lanthanum-strontium manganite (LSMO) (Franceschi et al., 2021); (c) STM image of a (2×5)-reconstructed SrTiO₃(110) surface (Riva et al., 2019); (d) SEM image of MgAl₂O₄.

vacuum mode, at 5 kV accelerating voltage and 7.4 mm working distance. Before the analysis, the solid was sputtered with Au:Pd 60:40 to create an 8 nm conductive layer to prevent electric charge build-up on the nonconductive sample, which could alter the secondary electron signal. Despite the sputtering, bright features caused by charging are observed, which could be due to the challenging deposition of the conductive layer on the irregular, porous surface.

Methods

Total variation

In 1992, Rudin, Osher, and Fatemi introduced the concept of total variation for image denoising (Rudin et al., 1992), which served as a prototype for many other models that followed (Chambolle and Pock, 2011; Bredies et al., 2010). The ROF model is a convex optimization problem with total variation as regularizer and a quadratic data fidelity term. In a discrete setting, for sufficiently smooth functions, the ROF model is defined as:

$$\min_u \left\{ \|\nabla u\|_{2,1} + \frac{\lambda}{2} \|u - f\|_2^2 \right\}, \quad (1)$$

where $u, f \in \mathbb{R}^{m \times n}$ are the sought solution and the input image respectively, $\|\nabla u\|_{2,1} = \sum_{i,j} |(\nabla u)_{i,j}|_2$, $|(\nabla u)_{i,j}|_2 = \sqrt{((\nabla u)_{i,j}^x)^2 + ((\nabla u)_{i,j}^y)^2}$ is the $L^{2,1}$ norm of ∇u , $\lambda > 0$ is a tuning parameter, and $\|u - f\|_2^2 = \sum_{i,j} |u_{i,j} - f_{i,j}|^2$ is the squared L^2 norm. The term $\|\nabla u\|_{2,1}$ is named the total variation

of u . Choosing the total variation as regularizer is a suitable choice for natural images since it allows the solution u to include sharp discontinuities like edges (e.g. object boundaries), offering a balance between feature preservation and noise removal.

Unfortunately, signals treated with the ROF model suffer from the so-called 'staircasing effect', where the output signal shows artificial flat areas. Several solutions have been proposed (Chambolle and Pock, 2011), and in this work we will discuss three of them.

The TV- L^1 model is obtained by substituting the squared L^2 norm with the L^1 norm in the data fidelity term of the ROF model:

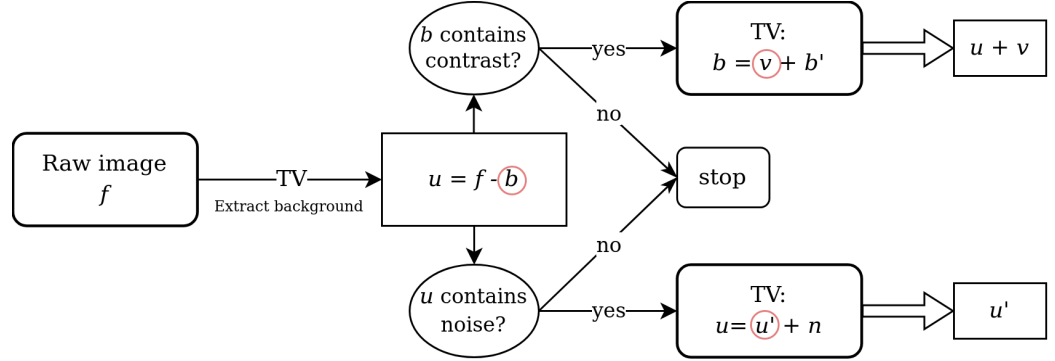
$$\min_u \{ \|\nabla u\|_{2,1} + \lambda \|u - f\|_1 \}, \quad (2)$$

where $\|u - f\|_1 = \sum_{i,j} |u_{i,j} - f_{i,j}|$. This simple change brings considerable advantages: this model is contrast invariant, more effective against salt&pepper noise, and preserves small features better than the ROF model also due to a minimal staircasing effect (Chan and Esedoglu, 2005; Nikolova, 2004). The Huber-ROF model (Zadorozhnyi et al., 2016) is another variant of the ROF model. It is obtained by substituting the L^1 norm of the total variation in Eq. 1 with the Huber norm:

$$|\nabla u|_\alpha = \begin{cases} \frac{|\nabla u|^2}{2\alpha} & \text{if } |\nabla u| \leq \alpha \\ |\nabla u| - \frac{\alpha}{2} & \text{if } |\nabla u| > \alpha \end{cases} \quad (3)$$

The parameter $\alpha > 0$ is introduced to define a tradeoff between the L^2 and L^1 norms as regularizers. This model allows for smoother solutions with very limited staircasing effect.

Fig. 2: Flowchart of the proposed workflow. Starting from the raw image f , its background b is extracted via TV minimization and u is calculated via subtraction. If b contains signal associated to prominent features' contrast v (e.g. from terraces or different terminations), the latter gets extracted from b and added to u . If u is affected by noise, the signal can be smoothed, obtaining u' . If both cases are present, one must first perform the contrast retrieval and then proceed with the smoothing. The red circles highlight the output from each TV minimization.



The last model we discuss is the (second order) Total Generalized Variation L^1 (TGV- L^1) (Bredies et al., 2010). The TGV- L^1 model consists in solving the problem

$$\min_{u,v} \left\{ \alpha_1 \|\nabla u - v\|_{2,1} + \alpha_2 \|\frac{1}{2}(\nabla + \nabla^T)v\|_{2,1} + \lambda \|u - f\|_1 \right\}, \quad (4)$$

where v is a vector field which minimizer value is located between 0 and ∇u , allowing for second order contributions. Qualitatively, the explanation is the following: near the edges $\nabla^2 u$ is larger than ∇u , so in order to minimize Eq. 4 having $v \sim 0$ is beneficial, and restores the standard TV regularization term; on the other hand, in smooth regions $\nabla^2 u$ will be low so it is beneficial to have $v \sim \nabla u$ in order to penalize the second derivatives. α_1, α_2 are control parameters. The first two terms of the sum are the (second order) total generalized variation of u , while the third one is the data fidelity term. As this model takes into account also the second derivatives of u (more details can be found at (Bredies et al., 2010)), images denoised with it look smoother than the ones with the above methods, given the absence of staircase effects. TV- L^1 and Huber-ROF have been implemented according to (Chambolle and Pock, 2011), while TGV- L^1 to (Knoll et al., 2011).

Workflow

An image f can be disassembled as a sum of its components $\{c_1, c_2, \dots, c_N\}$ (Fu et al., 2023):

$$f = \sum_{i=1}^N c_i.$$

This definition holds in general, but the problem is ill-posed since the number of components N is not specified a priori. Examples in literature decompose f in its structural and textural parts (Aujol et al., 2006), structural, oscillatory and smooth parts (Huska et al., 2021), or generally discuss about hierarchical image peeling (Fu et al., 2023).

Given the many possible ways a microscopy image can look like, we refrain from fixing a priori its number of components. Instead, we focus on illustrating through a workflow some cardinal examples and how tackle them. This workflow has been applied to the images discussed in this work, but the user can adapt it to their specific needs. The main steps of the workflow are summarized in Fig. 2. The first step consists in decomposing the raw image f in two parts b and u : b is the background, which includes low-frequency signals like tip scratches and other contrast variations (e.g. from terraces or different terminations); u encodes high-frequency components that define the edges of the image, like atomic arrangements, prominent structural features, or even noise. In the simplest of cases, performing this step is sufficient to obtain a clean image u . Optionally, a median filter with a 1×3 kernel is applied to u to remove horizontal pixel-thin scratches, frequently present in techniques such as ncAFM and STM. This process has been sufficient to clean the images in Fig. 1a, b.

If additional steps are required, we can have two other possible main cases. If the background b also contains relevant signal like the contrast between different terminations or terraces v , it is necessary to decompose b in two terms to obtain v , which will be added to u to obtain the final image. This strategy has been applied to Fig. 1c. If u is affected by noise, a second TV minimization can be performed to obtain a smoother, ideally noise-free version of u , here named u' . Fig. 1d has been cleaned with this procedure. Trivially, if an image is just affected by noise TV minimization can be applied to smoothen it and ideally remove the noise. Lastly, if an image contains both different-contrast areas and noise, one must first restore the contrast, then smoothen the final result.

Results and Discussion

This section presents and discusses the outcomes of our study. In the tuning process, each method involved adjusting only

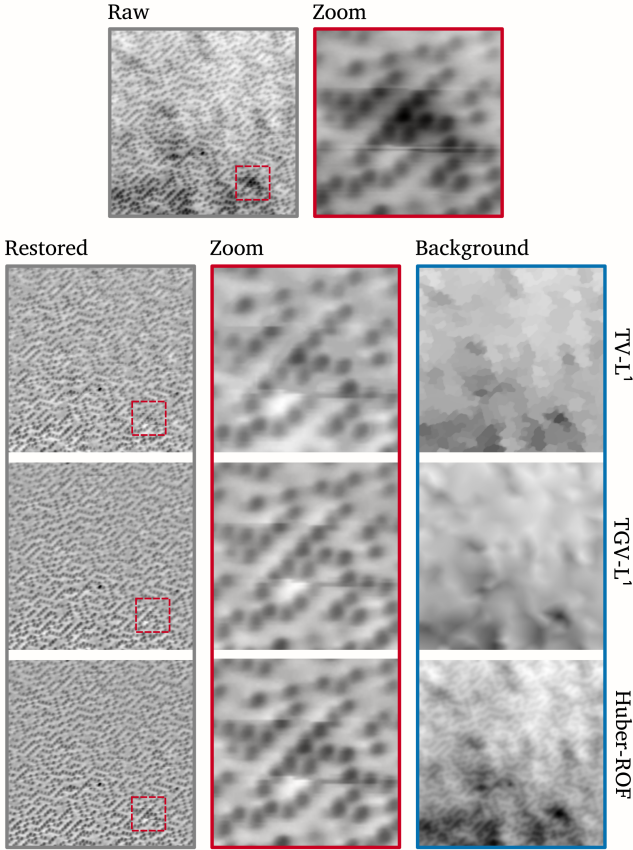


Fig. 3: Comparison between the background subtraction carried out with $TV-L^1$, $TGV-L^1$, and Huber-ROF on ncAFM image of K ions on mica presented in Fig. 1a. The Raw image and a zoomed area are compared with the Restored ones obtained from the background subtraction of the raw image; different backgrounds extracted via TV minimization are displayed in the right column. It is evident how differently the three methodologies perform. Huber-ROF is the most flexible method among the three, applicable to all the cases shown in this study, and it performs best in background extraction. The output for $TV-L^1$ has been obtained with $\lambda = 0.2$, the one for $TGV-L^1$ with $\lambda = 0.1$, and for Huber-ROF with $\lambda = 0.5$. A median filter with a 1×3 kernel has been applied to the restored images for all the three methods.

the λ parameter. The following parameters remained constant throughout the study: $\tau = 0.01$ (timestep related to the algorithm), $\alpha_1 = 1$, and $\alpha_2 = 2$ for $TGV-L^1$, while $\alpha = 0.05$ was consistently used for Huber-ROF. Notably, a more favorable outcome for Fig. 1d a better result was achieved with $\alpha = 0.005$. All calculations reached convergence with a Root Mean Square Error (RMSE) lower than $5 \cdot 10^{-6}$ between the background of the current iteration and the previous one.

In order to comprehend the domain of applicability of the various methods, it is crucial to compare their performances. Figure 3 illustrates the decomposition outcomes for Fig. 1a using three distinct TV methods. The output for $TV-L^1$ has been obtained with $\lambda = 0.2$, the one for $TGV-L^1$ with $\lambda = 0.1$, and for Huber-ROF with $\lambda = 0.5$.

Despite being a widely adopted method for TV denoising, the observations from Fig. 3 indicate that $TV-L^1$ is the least suitable among the methods investigated in this study for background subtraction. Even with a carefully chosen λ parameter, certain prominent dark spots within the non-uniform background persist, and undesired artifacts appear around the K ions, manifesting as distinct dark dots. As demonstrated in Fig. S1 in the Supplementary Material, increasing λ effectively removes the dark spots but excessively diminishes the contrast between K ions and the bright background, while also introducing new, unwanted artifacts. This behavior may be attributed to the L^1 norm as a fidelity term, known for its robustness against outliers, ultimately resulting in backgrounds comprised of spots with constant intensity rather than smoother, higher-detailed solutions.

$TGV-L^1$, incorporating second-order terms, facilitates smoother solutions by extracting more detailed backgrounds compared to first-order methods like $TV-L^1$ and Huber-ROF. In this case, no artifacts around the ions are introduced, and the contrast is largely preserved. While this outcome is desirable, Fig. S1 in the *Supplementary Material* indicates that varying λ for this method may excessively filter artifacts and noise, potentially yielding unsatisfactory results. For background extraction, achieving a balance in parameter selection is crucial to harness the benefits of $TGV-L^1$ without compromising on the preservation of relevant details.

In contrast, as observed in Fig. 3, Huber-ROF emerges as the most suitable algorithm for the designated tasks among the three. It excels in extracting the background without significantly diminishing the contrast of features, resulting in overall superior outcomes compared to $TV-L^1$ and $TGV-L^1$. Notably, the background achieved with Huber-ROF closely resembles the raw image, encompassing both the non-uniform background and signals from the K ions. While the latter is extracted and the contrast between the bright background and dark features is reduced, the denoised image maintains the sharpness of the features. Adjusting the parameter λ also yields more controlled solutions compared to $TV-L^1$ and $TGV-L^1$. It is also worth mentioning that, depending on the algorithm, parameters, and image used, the computational time varies. $TV-L^1$ and Huber-ROF, being first-order methods, are generally faster than $TGV-L^1$, which is a higher-order one. Increasing lambda decreases the computational time, as the output (i.e. the background) more resembles to the input image. The details and scale of the input image also influence the time factor: larger, more detailed images generally take more time than smaller, less detailed ones. For these reasons, the computational time can go from a fraction of a second to the order of minutes.

Figure 4 further illustrates the dependence of Huber-ROF on λ , applied to the same image as in Fig. 3. Increasing λ allows to extract features of smaller and smaller scale, going from a larger-scale background to a small-scale signal associated with the atoms; for this reason, it must be selected for background extraction without excessively altering the topographical features of the image (e.g. related to the atomic arrangements). For $\lambda \leq 0.1$ the effects are minimal and do not lead to satisfactory results as the non-uniform background is still present. From $\lambda \geq 0.5$ the dark spots are mostly removed. For $\lambda = 0.5$ we observe how the non-uniform background is removed without affecting the signal coming from the K ions. We argue that the optimal value for λ in this case lies between 0.5 and 1 since for the latter the dark halos

surrounding the K ions are extracted as well, but their sharpness is preserved. Setting $\lambda = 10$ removes the background but decreases the overall contrast: the single atoms preserve their sharpness, but the excessive subtraction flattens the signal too much, giving the image an unnatural dark-gray background. For purely denoising purposes that aim to preserve the images' original appearance this is negative, but if the task requires highlighting or isolating atomic features like K ions, selecting a high value of λ might be beneficial. Further discussions of parameter selection can be found in (Chan and Esedoglu, 2005). As highlighted in that work, TV- L^1 has a clear geometric interpretation related to size selection: this is made evident in Fig. S1 in the Supplementary material, where the output of different λ values is compared. TV- L^1 and TGV- L^1 qualitatively follow the same behavior, but we have not found an automated way to estimate the parameters λ and α . Figs. 4 and S1 however give a good insight on parameter selection, which proved to be sufficient during internal tests with different images.

Figure 5 shows the application of Huber-ROF to the STM image of LSMO(110) presented in Fig. 1b and addresses how to operate in case of evident horizontal lines. Building on the favorable outcomes observed in our previous results, Huber-ROF is chosen for its capability to extract the background while minimizing the inclusion of signals from atomic features. This ensures the preservation of the original topography of the surface despite the presence of distinct horizontal lines. In the case of K ions on mica (Fig. 1a), the unwanted signal appears as dark and bright spots non-uniformly distributed, removable by applying TV minimization to both vertical and horizontal directions. In the case shown in Figure 5a the background is made of perfectly horizontal lines, parallel to the scanning direction; the correct strategy here is to apply TV minimization only along the horizontal direction, ignoring the vertical sharp signal gradients due to the presence of bright lines. Since these lines only slightly vary in intensity along the horizontal direction, they can be seen as 'large-scale objects' and thus require setting a low λ to avoid extracting the underneath texture, as discussed in Fig. 4. $\lambda = 0.05$ has been set for this purpose. The background in panel b) indeed shows how the lines were accurately extracted, alongside only some signal coming from the bright protrusions. The result in panel c) is the optimal one from this image, since not only the horizontal lines have been removed, but also the bright atomic features show a higher contrast than before, and their sharpness is preserved; the zoomed areas in panels d), e) highlight this fact. To visualize how the signal looks in panels a), b), and c), a line profile is shown in panel f). A line profile consists of plotting the signal coming from the image as a function of coordinates, highlighted by a line overlaying the image. In our case, this allows to visualize the peak distribution coming from the atomic rows. The dashed line associated with the raw image consists of peaks distributed without regularity due to the horizontal lines, covering the periodic pattern underneath. The dotted line, associated with the background, shows that the most prominent peaks are due to the bright lines. The full line shows the periodic signal coming from the atomic rows. In summary, the restoration process successfully preserved the topography of the image, retaining the bright atomic rows, even brighter adsorbates, and darker signals originally present. This affirms the effectiveness of the Huber-ROF method, with an observed increase in the contrast of the features.

When terraces or terminations with different levels of contrast are present, the restoration process needs one extra step, as explained in the *Methods* section and Fig. 2. Figure 6 shows

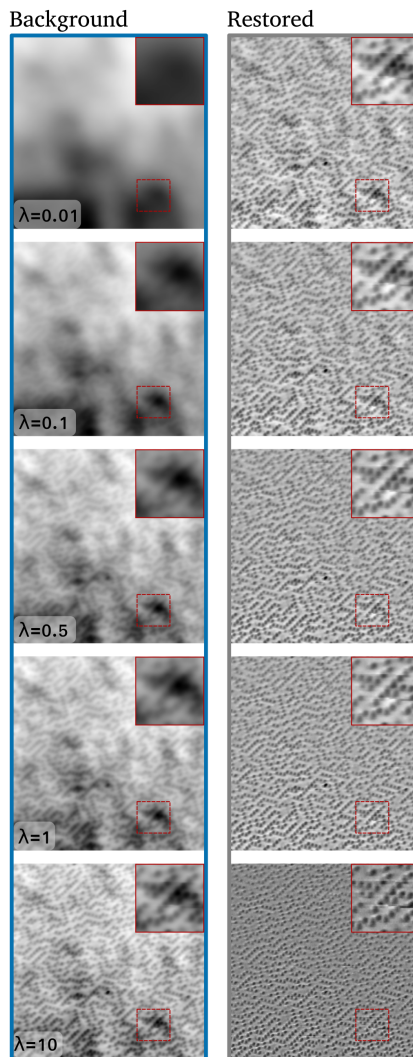


Fig. 4: Background and restored image as a function of λ using Huber-ROF. Raw image in Fig. 1a. Increasing λ allows to filter smaller-sized features. The optimal λ value lies between 0.5 and 1, where the background is removed without compromising the contrast. $\lambda = 10$ shows that setting this parameter too high excessively reduces the contrast between K ions and the background. This might be beneficial for some tasks that require a clear imaging of the atoms or structures, but for pure restoration purposes it is advised to preserve the original features as much as possible. A median filter with a 1×3 kernel has been applied to the restored images.

the restoration of an STM image of a (2×5) -reconstructed SrTiO₃(110) surface using Huber-ROF with $\lambda = 0.05$ for both background extraction and background blurring. In this case, extracting the background with TV minimization removes the contrast between the terraces, resulting in the image labeled as 'Flat' (6b), where features belonging to different terraces or terminations display roughly the same intensity. The method we propose to recover the original contrast between terraces or terminations consists, with a second step, of applying TV on the extracted background (6c) and obtaining what we label as 'Smooth

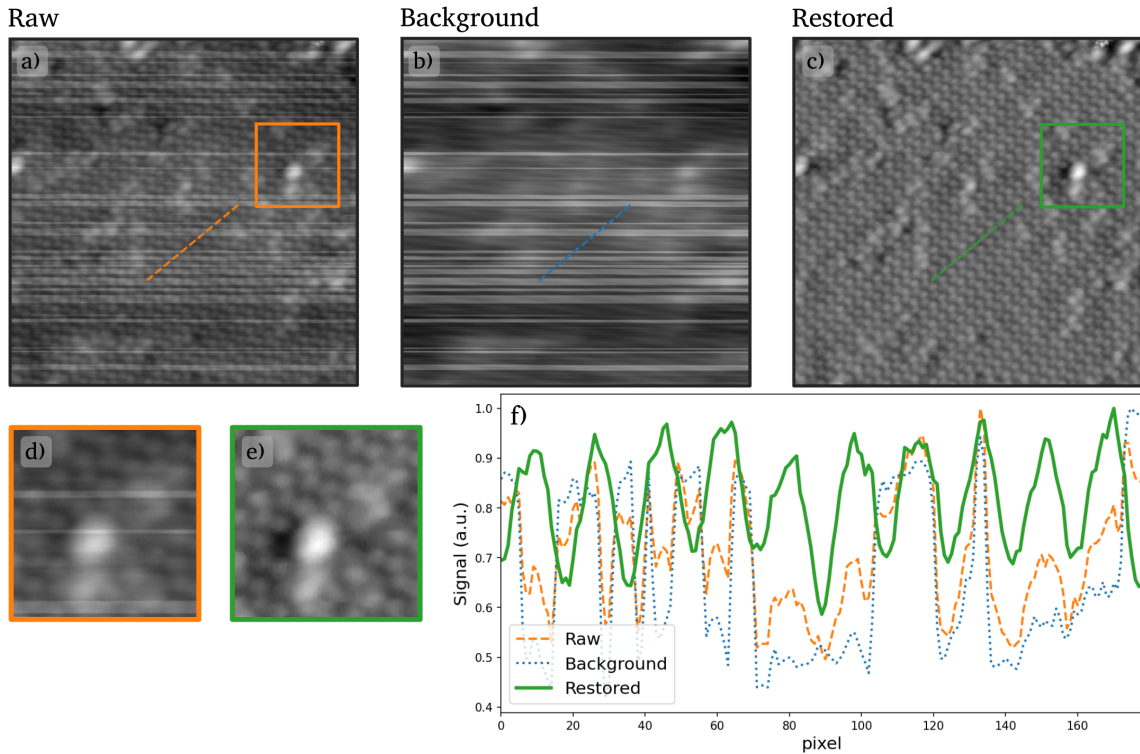


Fig. 5: Background subtraction of the STM image of LSMO(110) presented in Fig. 1b via Huber-ROF method, with $\lambda = 0.05$. The image is corrupted by visible bright, horizontal lines. (a) raw image overlaid with a dashed line and the region highlighted in panel (d); (b) background extracted via TV minimization overlaid with a dashed line; (c) restored image obtained via background subtraction of the raw image, overlaid with a dashed line and the region highlighted in panel (e); (d), (e) zoomed regions of panels (a), (c) respectively; (f) line profiles relative to the lines overlaying panels (a), (b), and (c), each one normalized to the maximum signal intensity of the image they refer to, for comparison purposes. A median filter with a 1×3 kernel has been applied to the restored image.

background’: this extra step aims to remove the horizontal lines from the background, obtaining a smoother version of it that preserves the contrast between terraces, as can be observed in panel 6d. What is shown in Fig. 6c and Fig. 6d is comparable to applying a highpass and then a lowpass filter, respectively. The line profiles associated with the raw, flat, and restored (6f) images are shown in panel 6e. The raw image exhibits a modest contrast between bright features and the background but displays a distinct contrast between the terraces. In the flattened image, the contrast between terraces is almost absent, although the bright and dark features become more prominent. Incorporating the smoother background slightly reduces the overall contrast but significantly restores the original contrast between terraces. The dark, horizontal lines have been removed. However, dark shades in the upper and lower parts of the image persist.

Figure 7 presents the restoration outcomes for a SEM image of MgAl_2O_4 . In contrast to the previous example, this image not only features bright lines parallel to the scanning direction but also exhibits low shot noise. While background subtraction effectively addresses the horizontal lines (low-frequency signal), an additional step is required to eliminate the other noise component, whether it be shot noise, Gaussian noise, salt&pepper noise, or a similar type. Typically, Gaussian and shot noise can be removed via low-pass filtering, salt&pepper noise via median filtering, and low-frequency background with high-pass filtering,

but TV can cope with all of them depending on the setup of λ ; Fig. S2 in the *Supplementary material* shows a comparison between images cleaned with our proposed workflow, and with well-known filtering techniques implemented in ImageJ. The two methodologies, albeit based on different theoretical backgrounds, show reciprocal consistency. As previously stated in Fig. 5, Huber-ROF applied to the horizontal direction is optimal to remove the bright lines, and the results of background subtraction are shown in Figure 7b. The median filter applied to the vertical direction smoothed the features’ edges by decreasing the small scan instability. Except for some bright areas, the lines have been removed. To eliminate noise present in the image, $\text{TGV-}L^1$ is subsequently applied to the image in panel b), obtaining what is shown in panel c): most of the leftover noise has been removed, and the edges have been preserved. We clarify that in such scenario low shot noise is not strictly necessary to remove, but we decided to perform this additional step for demonstration purposes of the well-known denoising capabilities of TV. The overall results show how the depth and details of the image are slightly reduced with respect to the raw image, and some bright areas are still present; the latter are flat, bright signals that do not encode physical information about the system, and their hypothetical removal will not reveal any hidden detail.

When images are heavily afflicted by shot noise or similar, it is sufficient to apply TV denoising to directly obtain the clean

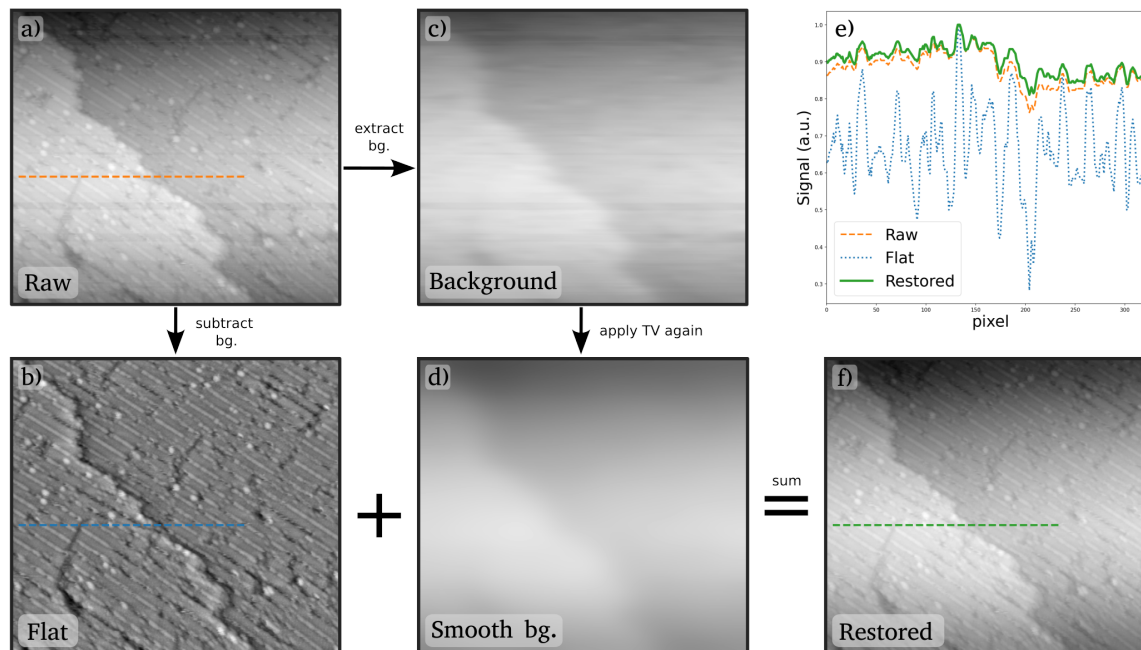


Fig. 6: Restoration of the STM image of a (2×5) -reconstructed $\text{SrTiO}_3(110)$ surface displayed in Fig. 1c, following the steps described in the *workflow* subsection, using the Huber-ROF method with $\lambda = 0.05$ for both background extraction and background blurring. These steps are required when the image contains different terminations, terraces, or in general topographically equivalent areas with different contrasts. (a) raw image; (b) flat image obtained with background subtraction; (c) background extracted with TV minimization; (d) smooth background, obtained by applying TV denoising on the background shown in (c); (e) line profiles relative to raw, flat and denoised images; each line profile is normalized to the maximum signal intensity of the image they refer to, for comparison purposes; (f) restored image.

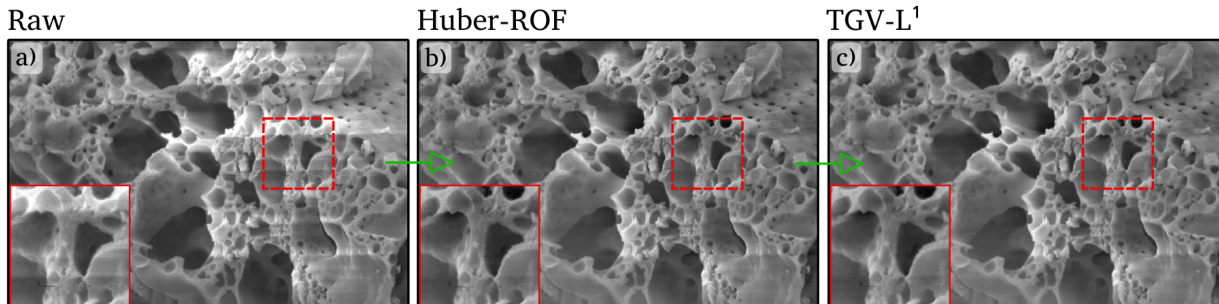


Fig. 7: Restoration steps for the SEM image of MgAl_2O_4 shown in Fig. 1d, with the steps described in the *Workflow* subsection. The image is corrupted by bright, horizontal lines and low shot noise, which are removed with two different denoising steps. (a) Raw image and magnified region as inset; (b) image cleaned with Huber-ROF ($\lambda = 0.001$, $\alpha = 0.005$), which removed most of the horizontal lines, with a magnified region as inset; (c) after applying Huber-ROF, $\text{TGV-}L^1$ has been applied to remove the low shot noise affecting the image, using $\lambda = 1.5$.

image u . As TV denoising is not the main focus of this work, but rather its image decomposition capabilities, we decided to show this scenario in the *Supplementary material*, where we tested the denoising capabilities of $\text{TGV-}L^1$ against high shot noise present in a STEM image of graphene (Fig. S2b) and simulated MoS_2 STEM images (more informations on Fig. S3).

Summary and Conclusions

This work presents a total variation-based workflow to restore microscopy images by performing background subtraction and denoising. Five different study cases have been proposed taken from AFM, STM, SEM, and STEM images. The Huber-ROF, $\text{TV-}L^1$, and $\text{TGV-}L^1$ methods have been applied. For background subtraction, the Huber-ROF method is the most flexible one among the three since it allows with the sole control of the λ parameter to filter out signals of different sizes, extracting

the background from the raw image with great control. The TGV- L^1 method is confirmed to be the most edge-preserving one among the three, and it is suited for denoising but less for background extraction. TV- L^1 proved to be not enough sensitive to small features like atoms, making it unsuitable for background subtraction but still usable for texture smoothing (even though TGV- L^1 outperforms it).

Our workflow mainly focuses on background subtraction, proven to be particularly suitable for images displaying tip changes or sudden contrast variations due to tip-sample interactions, imaged as bright or dark lines parallel to the scanning direction. In the case of Gaussian noise or similar, obtaining a clean image directly from TV minimization is recommended, as shown in the case of the SEM image of MgAl_2O_4 and the simulated STEM images of MoS_2 in the supplementary materials.

A second processing step is required in cases when the image contains terraces or different terminations, which display different signal intensities: this is necessary to remove the small-scale noise from the background, ideally keeping the original contrast between terraces or terminations. The method proved effective but we have not found a way to remove possible signal modulations not associated with the terraces or terminations. In the third case we have discussed the image contains both horizontal bright or dark lines and Gaussian-like noise. The two-steps process consists first in removing the horizontal lines through background subtraction, then denoising the resulting image using preferably TGV- L^1 .

The positive outcomes of this study suggest a wider degree of applicability of this workflow to other types of images. The code, alongside the results shown in this work, is publicly available on GitHub as a part of the AiSurf package (Corrias et al., 2023), an open-access tool to clean and analyze microscopy images without requiring extensive knowledge of the user in the field. This workflow is conceived for single or multiple image denoising; it can be integrated into automated experimental workflows or used as a standalone code to denoise noisy image datasets. For denoising purposes, many different methods have been proposed to automate the choice of λ (Goyal et al., 2020; Pan et al., 2019; Langer, 2017; Selesnick et al., 2014), however, to the best of our knowledge, there seem to be no suitable methods for background extraction; this might be due to the difficulty of giving a formal definition of background, which is mostly vague, case-dependent and not describable by means of a model. Developing a robust method to select λ will be considered as a future outlook. The comparison with manually filtered images also shows the consistency of TV restoration with other techniques, which have shown equally-positive results.

Data availability statement

The AiSurf package, including the code used for this study, can be accessed from <https://github.com/QuantumMaterialsModelling/AiSurf-Automated-Identification-of-Surface-images>.

Acknowledgments

We are grateful to Michael Schmid for insightful discussions and for his critical reading of the manuscript. We kindly thank Jacob Madsen and Toma Susi for the insights and technical discussions about STEM, which contributed to enriching this work. We thank the technician Karin Withmore for helping us clarify some

technicalities of the SEM apparatus used to acquire Fig. 1d. This research was funded in whole or in part by the Austrian Science Fund (FWF) 10.55776/F81. For Open Access purposes, the author has applied a CC BY public copyright license to any author-accepted manuscript version arising from this submission.

Conflict of Interest

The authors have no conflicts of interest to declare. MC executed the research and made the main contribution to writing the article. GF, MR, AT, and KF contributed to providing and describing the experimental images. UD, TP and CF supervised the research and constantly revised the article. All authors discussed the article during each step, providing their feedback and supervision.

References

- Abràmoff, M. D., P. J. Magalhães, and S. J. Ram (2004). Image processing with imageJ. *Biophotonics international* 11(7), 36–42.
- Alvarado, W., V. Agrawal, W. S. Li, V. P. Dravid, V. Backman, J. J. de Pablo, and A. L. Ferguson (2023, Jun). Denoising autoencoder trained on simulation-derived structures for noise reduction in chromatin scanning transmission electron microscopy. *ACS Central Science* 9(6), 1200–1212.
- Aujol, J.-F., G. Gilboa, T. Chan, and S. Osher (2006, Apr). Structure-texture image decomposition—modeling, algorithms, and parameter selection. *Int. J. Comp. Vis.* 67(1), 111–136.
- Belianinov, A., Q. He, M. Kravchenko, S. Jesse, A. Borisevich, and S. V. Kalinin (2015, Jul). Identification of phases, symmetries and defects through local crystallography. *Nat. Comm.* 6(1), 7801.
- Binnig, G., H. Rohrer, C. Gerber, and E. Weibel (1982, Jul). Surface studies by scanning tunneling microscopy. *Phys. Rev. Lett.* 49, 57–61.
- Biswas, A., M. Ziatdinov, and S. V. Kalinin (2023, oct). Combining variational autoencoders and physical bias for improved microscopy data analysis. *Mach. Learn.: Sci. Technol.* 4(4), 045004.
- Bredies, K., K. Kunisch, and T. Pock (2010). Total generalized variation. *SIAM J. Imag. Sci.* 3(3), 492–526.
- Cai, X., R. Chan, C.-B. Schonlieb, G. Steidl, and T. Zeng (2019). Linkage between piecewise constant Mumford–Shah model and Rudin–Osher–Fatemi model and its virtue in image segmentation. *SIAM J. Sci. Comp.* 41(6), B1310–B1340.
- Chambolle, A., V. Caselles, D. Cremers, M. Novaga, T. Pock, et al. (2010). An introduction to total variation for image analysis. *Th. found. num. meth. sparse recovery* 9(263-340), 227.
- Chambolle, A. and T. Pock (2011, May). A first-order primal-dual algorithm for convex problems with applications to imaging. *J. Math. Imaging. Vis.* 40(1), 120–145.
- Chan, T. F. and S. Esedoglu (2005). Aspects of total variation regularized L1 function approximation. *SIAM J. Appl. Math.* 65(5), 1817–1837.
- Chang, C.-W. and M.-A. Mycek (2012). Total variation versus wavelet-based methods for image denoising in fluorescence lifetime imaging microscopy. *J. Biophotonics* 5(5-6), 449–457.
- Chen, X., M. Ding, X. Wang, Y. Xin, S. Mo, Y. Wang, S. Han, P. Luo, G. Zeng, and J. Wang (2024, Jan). Context autoencoder for self-supervised representation learning. *132*(1), 208–223.
- Collins, T. J. (2007). ImageJ for microscopy. *Biotechniques* 43(S1), S25–S30. PMID: 17936939.
- Corrias, M., L. Papa, I. Sokolović, V. Birschitzky, A. Gorfer, M. Setvin, M. Schmid, U. Diebold, M. Reticcioli, and C. Franchini (2023). Automated real-space lattice extraction for atomic force microscopy images. *Mach. Learn.: Sci. Technol.* 4(1), 015015.
- Dürig, U., J. K. Gimzewski, and D. W. Pohl (1986, Nov). Experimental observation of forces acting during scanning tunneling microscopy. *Phys. Rev. Lett.* 57, 2403–2406.
- Elad, M., B. Kowar, and G. Vaksman (2023). Image denoising: The deep learning revolution and beyond—a survey paper. *SIAM J. Imag. Sci.* 16(3), 1594–1654.
- Fan, L., F. Zhang, H. Fan, and C. Zhang (2019). Brief review of image denoising techniques. *Vis. Comp. Industry, Biomedicine, and Art* 2, 1–12.
- Franceschi, G., P. Kocán, A. Conti, S. Brandstetter, J. Balajka, I. Sokolović, M. Valtiner, F. Mittendorfer, M. Schmid, M. Setvín, et al. (2023, Jan). Resolving the intrinsic short-range ordering of K⁺ ions on cleaved muscovite mica. *Nat. Comm.* 14(1), 208.
- Franceschi, G., M. Schmid, U. Diebold, and M. Riva (2021, Sep). Two-dimensional surface phase diagram of a multicomponent perovskite oxide: La_{0.8}Sr_{0.2}MnO₃(110). *Phys. Rev. Mater.* 5, L092401.
- Franchini, C., M. Reticcioli, M. Setvin, and U. Diebold (2021). Polarons in materials. *Nat. Rev. Mat.* 6(7), 560–586.
- Fu, Y., J. Ma, and X. Guo (2023). Hierarchical image peeling: A flexible scale-space filtering framework. *235*, 103769.
- Giessibl, F. J. (2003, Jul). Advances in atomic force microscopy. *Rev. Mod. Phys.* 75, 949–983.
- Giessibl, F. J. (2019, 01). The qPlus sensor, a powerful core for the atomic force microscope. *Rev. Scient. Instr.* 90(1), 011101.
- Goyal, B., A. Dogra, S. Agrawal, B. S. Sohi, and A. Sharma (2020). Image denoising review: From classical to state-of-the-art approaches. *Info. fusion* 55, 220–244.
- Hapala, P., M. Ondráček, O. Stetsovych, M. Švec, and P. Jelínek (2015). Simultaneous nc-AFM/STM measurements with atomic resolution. *Noncontact At. Force Microsc.: Vol. 3*, 29–49.
- Horcas, I., R. Fernández, J. M. Gómez-Rodríguez, J. Colchero, J. Gómez-Herrero, and A. M. Baro (2007, 01). WSXM: A software for scanning probe microscopy and a tool for nanotechnology. *Rev. Sci. Instr.* 78(1), 013705.
- Huska, M., S. H. Kang, A. Lanza, and S. Morigi (2021). A variational approach to additive image decomposition into structure, harmonic, and oscillatory components. *SIAM J. Imag. Sci.* 14(4), 1749–1789.
- Inkson, B. (2016). Scanning electron microscopy (SEM) and transmission electron microscopy (TEM) for materials characterization. In G. Hübschen, I. Altpeter, R. Tschuncky, and H.-G. Herrmann (Eds.), *Materials Characterization Using Nondestructive Evaluation (NDE) Methods*, pp. 17–43. Woodhead Publishing.
- Kalinin, S., C. Ophus, P. M. Voyles, R. Erni, D. Kepaptsoglou, V. Grillo, A. R. Lupini, M. P. Oxley, E. Schwenker, M. K. Chan, et al. (2022, Mar). Machine learning in scanning transmission electron microscopy. *Nat. Rev. Methods Primers* 2(1), 11.
- Kalinin, S., M. Ziatdinov, J. Hinkle, S. Jesse, A. Ghosh, K. P. Kelley, A. R. Lupini, B. G. Sumpter, and R. K. Vasudevan (2021, Aug). Automated and autonomous experiments in electron and scanning probe microscopy. *ACS Nano* 15(8), 12604–12627.
- Kalinin, S. V., R. Vasudevan, Y. Liu, A. Ghosh, K. Roccapriore, and M. Ziatdinov (2023). Probe microscopy is all you need. *Mach. Learn.: Sci. Technol.* 4(2), 023001.
- Kaur, P., G. Singh, and P. Kaur (2018). A review of denoising medical images using machine learning approaches. *Curr. Med. Imaging* 14(5), 675–685.
- Kawahara, K., R. Ishikawa, S. Sasano, N. Shibata, and Y. Ikuhara (2022, 06). Atomic-resolution STEM image denoising by total variation regularization. *Microsc.* 71(5), 302–310.
- Kingma, D. P. and M. Welling (2019). An introduction to variational autoencoders. *Foundations and Trends[®] in Machine Learning* 12(4), 307–392.
- Knoll, F., K. Bredies, T. Pock, and R. Stollberger (2011). Second order total generalized variation (TGV) for MRI. *Magn. Reson. Med.* 65(2), 480–491.

- Kraushofer, F., N. Resch, M. Eder, A. Rafsanjani-Abbasi, S. Tobisch, Z. Jakub, G. Franceschi, M. Riva, M. Meier, M. Schmid, et al. (2021). Surface reduction state determines stabilization and incorporation of Rh on α -Fe₂O₃ (1 $\bar{1}$ 02). *Adv. Mater. Interfaces* 8(8), 2001908.
- Langer, A. (2017). Automated parameter selection for total variation minimization in image restoration. *J. Math. Imag. Vis.* 57, 239–268.
- Leitherer, A., B. Yeo, C. Liebscher, and L. Ghiringhelli (2023, Oct). Automatic identification of crystal structures and interfaces via artificial-intelligence-based electron microscopy. *npj Comp. Mat.* 9(1), 179.
- Liao, C.-S., J. H. Choi, D. Zhang, S. H. Chan, and J.-X. Cheng (2015, Aug). Denoising stimulated Raman spectroscopic images by total variation minimization. *J. of Phys. Chem. C* 119(33), 19397–19403.
- Lin, R., R. Zhang, C. Wang, X.-Q. Yang, and H. L. Xin (2021, Mar). TEMImageNet training library and atomSegNet deep-learning models for high-precision atom segmentation, localization, denoising, and deblurring of atomic-resolution images. *Sci. Rep.* 11(1), 5386.
- Liu, J., Y. Sun, X. Xu, and U. S. Kamilov (2019). Image restoration using total variation regularized deep image prior. In *ICASSP 2019 - 2019 IEEE International Conference on Acoustics, Speech and Signal Processing (ICASSP)*, pp. 7715–7719.
- Madsen, J., P. Liu, J. Kling, J. B. Wagner, T. W. Hansen, O. Winther, and J. Schiøtz (2018). A deep learning approach to identify local structures in atomic-resolution transmission electron microscopy images. *Adv. Theory Simul.* 1(8), 1800037.
- Majzik, Z., B. Drevniok, W. Kaminski, M. Ondracek, A. B. McLean, and P. Jelinek (2013). Room temperature discrimination of adsorbed molecules and attachment sites on the Si (111)-7 \times 7 surface using a qplus sensor. *ACS nano* 7(3), 2686–2692.
- Majzik, Z., M. Tchalala, M. Švec, P. Hapala, H. Enriquez, A. Kara, A. Mayne, G. Dujardin, P. Jelínek, and H. Oughaddou (2013, may). Combined AFM and STM measurements of a silicene sheet grown on the Ag(111) surface. *J. Phys.:Condens. Matter* 25(22), 225301.
- Meier, M., J. Hulva, Z. Jakub, F. Kraushofer, M. Bobić, R. Bliem, M. Setvín, M. Schmid, U. Diebold, C. Franchini, and G. S. Parkinson (2022). CO oxidation by Pt₂/Fe₃O₄: Metastable dimer and support configurations facilitate lattice oxygen extraction. *Sci. Adv.* 8(13), eabn4580.
- Meinel, W., J.-C. Olivo-Marin, and E. D. Angelini (2018). Denoising of microscopy images: A review of the state-of-the-art, and a new sparsity-based method. *IEEE Transactions Imag. Proces.* 27(8), 3842–3856.
- Morita, S., F. Giessibl, E. Meyer, and R. Wiesendanger (2015). *Noncontact Atomic Force Microscopy: Volume 3*. Nanosci. Nanotechnol. Springer International Publishing.
- Nikolova, M. (2004, Jan). A variational approach to remove outliers and impulse noise. *J. Math. Imag. Vis.* 20(1), 99–120.
- Nord, M., P. E. Vullum, I. MacLaren, T. Tybell, and R. Holmestad (2017, Feb). Atomap: a new software tool for the automated analysis of atomic resolution images using two-dimensional gaussian fitting. *Adv. Struct. Chem. Imaging* 3(1), 9.
- Pan, H., Y.-W. Wen, and H.-M. Zhu (2019). A regularization parameter selection model for total variation based image noise removal. *Appl. Math. Model.* 68, 353–367.
- Pavliček, N. and L. Gross (2017). Generation, manipulation and characterization of molecules by atomic force microscopy. *Nat. Rev. Chem.* 1(5), 1–11.
- Potapov, P. and A. Lubk (2019, Apr). Optimal principal component analysis of STEM XEDS spectrum images. *Adv. Struct. Chem. Imaging* 5(1), 4.
- Pregowska, A., A. Roszkiewicz, M. Osial, and M. Giersig (2024). How scanning probe microscopy can be supported by artificial intelligence and quantum computing? *Microsc. Res. Tech.* 87(11), 2515–2539.
- Reticcioli, M., I. Sokolović, M. Schmid, U. Diebold, M. Setvín, and C. Franchini (2019, Jan). Interplay between adsorbates and polarons: CO on rutile TiO₂(110). *Phys. Rev. Lett.* 122, 016805.
- Riva, M., G. Franceschi, Q. Lu, M. Schmid, B. Yildiz, and U. Diebold (2019, Apr). Pushing the detection of cation nonstoichiometry to the limit. *Phys. Rev. Mater.* 3, 043802.
- Rudin, L. I., S. Osher, and E. Fatemi (1992). Nonlinear total variation based noise removal algorithms. *60(1)*, 259–268.
- Selesnick, I. W., H. L. Graber, D. S. Pfeil, and R. L. Barbour (2014). Simultaneous low-pass filtering and total variation denoising. *IEEE Trans. Sign. Process.* 62(5), 1109–1124.
- Sokolović, I., M. Reticcioli, M. Čalkovský, M. Wagner, M. Schmid, C. Franchini, U. Diebold, and M. Setvín (2020). Resolving the adsorption of molecular O₂ on the rutile TiO₂(110) surface by noncontact atomic force microscopy. *Proc. Natl. Acad. Sci.* 117(26), 14827–14837.
- Spadafora, E., J. Berger, P. Mutombo, M. Telychko, M. Svec, Z. Majzik, A. McLean, and P. Jelínek (2014). Identification of surface defects and subsurface dopants in a delta-doped system using simultaneous nc-AFM/STM and DFT. *J. Phys. Chem. C* 118(29), 15744–15753.
- Stetsovych, O., M. Todorović, T. K. Shimizu, C. Moreno, J. W. Ryan, C. P. León, K. Sagisaka, E. Palomares, V. Matolín, D. Fujita, et al. (2015). Atomic species identification at the (101) anatase surface by simultaneous scanning tunnelling and atomic force microscopy. *Nat. comm.* 6(1), 7265.
- Taherkhani, F., M. J. R. Fatemi, and Y. Ganjdanesh (2016). Linear filtering and total variation de-noising of composite noises: Different architectures and simulation study. *J. of Circuits and Systems* 4, 55.
- Tersoff, J. and D. R. Hamann (1985, Jan). Theory of the scanning tunneling microscope. *Phys. Rev. B* 31, 805–813.
- Thakur, R. S., S. Chatterjee, R. N. Yadav, and L. Gupta (2021). Image de-noising with machine learning: A review. *IEEE Access* 9, 93338–93363.
- Wang, F., T. R. Henninen, D. Keller, and R. Erni (2020, Oct). Noise2Atom: unsupervised denoising for scanning transmission electron microscopy images. *Appl. Microsc.* 50(1), 23.
- Wang, M., Q. Wang, J. Chanussot, and D. Li (2021). Hyperspectral image mixed noise removal based on multidirectional low-rank modeling and spatial-spectral total variation. *59(1)*, 488–507.
- Wang, Y., H. Zhou, et al. (2006). Total variation wavelet-based medical image denoising. *Int. J. Biom. Imag.* 2006(1), 089095.
- Werlberger, M., T. Pock, and H. Bischof (2010). Motion estimation with non-local total variation regularization. In *2010 IEEE Computer Society Conference on Computer Vision and Pattern Recognition*, pp. 2464–2471.
- Zadorozhnyi, O., G. Benecke, S. Mandt, T. Scheffer, and M. Kloft (2016). Huber-norm regularization for linear prediction models.

- In *Mach. Learn. Knowledge Discovery in Databases*, Cham, pp. 714–730. Springer International Publishing.
- Zhang, C., R. Han, A. R. Zhang, and P. Voyles (2020). Denoising atomic resolution 4D scanning transmission electron microscopy data with tensor singular value decomposition. *Ultramicroscopy* 219, 113123.
- Ziletti, A., D. Kumar, M. Scheffler, and L. M. Ghiringhelli (2018, Jul). Insightful classification of crystal structures using deep learning. *Nat. Comm.* 9(1), 2775.